Rapid #: -11349382

Experimental Investigation of Circular Reinforced Concrete Columns under Different Loading Histories

Wei-Jian Yi, Yun Zhou, Yi Liu & Liwei Liu

Taylor & Francis
Taylor & Francis Group

Experimental Investigation of Circular Reinforced Concrete Columns under Different Loading Histories

WEI-JIAN YI[1], YUN ZHOU[1], YI LIU[2], and LIWEI LIU[1]

[1]College of Civil Engineering, Hunan University, Changsha, Hunan Province, P. R. China
[2]Hunan Provinces Architectural Design Institute, Changsha, Hunan Province, P. R. China

Three reinforced concrete (RC) circular column specimens without an effective concrete cover were tested under constant axial compressive as well as cyclic lateral loading. The seismic behavior of the specimens under different loading paths was examined with the objective of understanding the influence of displacement history sequence on the seismic behavior of the columns in near-fault earthquakes. The influence of displacement history sequence upon the hysteretic characteristics, stiffness degradation, lateral capacity, as well as energy dissipation analysis was conducted. The hoop strains of lateral reinforcement at varied column heights under cyclic loading were attained by means of 8–16 strain gauges attached along the hoops. Additionally, the characteristics of strain distribution were investigated in the transverse reinforcement. The results of strain distribution were evaluated with Mander's confinement stress model and the distribution around the cross section. The length of the plastic hinge at the end of the specimen was evaluated by measurement as well as the inverse analysis. Finally, the deformation of the specimen, which includes the components of shear deformation, bending deformation and bonding-slip deformation, was evaluated and successfully separated.

1. Introduction

Near-fault ground motion recorded in recent years (1994 Northridge, 1995 Kobe, and 1999 Chi-Chi) has provided clear evidence that the near-field earthquakes may lead a serious damage to the reinforced concrete (RC) structures, and the impulsive load is unique compared with the far-fault earthquakes. Near-fault ground motions differ from far-field ground motions in that they often contain a long-period, high-velocity pulse in the fault-normal direction and permanent ground displacement [Somerville, 2002]. The high amplitude pulse is attributed to the near-fault forward directivity effect, which is the result of the fault rupture velocity being approximately equal to the shear wave velocity. At the same time, most of the energy was produced with high amplitude pulse at the site in a short duration [Austin, 2009]. The largest deformation demands in the earthquake are associated with the first fewer reversed cycles of impulse loading [Kalkan and Kunnath, 2006]. In the near-fault earthquakes, the spectra were different from which in normal

ground motions, and the velocity-sensitive region in near-fault motion spectra is much narrower than the far-field motion [Chopra and Chintanpakdee, 2001]. Liu [2010] revealed that the RC frame structures designed based on current design spectrum are inadequate for around 70% ground motion records considering the near-fault effects. In addition, larger-story drift angles beyond the limits in provisions will be resulted when PGV/PGA is over 0.2. Energy caused by the impulsive ground motion of the structure will lead to a strong ductility demand on multistory structures [Hall *et al.*, 1995].

In the past few decades, although some studies on the seismic performance of RC columns under the pulse-like ground motions were conducted, few tests resulted in consistent each other. Pujol *et al.* [2006] tested 16 RC columns with rectangular section were tested in the laboratory by Pujol *et al.* [2006]. It was found that displacement history before the yielding point of the column was found no influence on the capacity of the specimen, while the drift capacity correlated with the amplitudes and number of cycles. In contrast, Hwang [1984] argued that the impulsive loading showed no effect on the displacement ductility capacity for flexural column. This argument was consistent with that of Hamilton *et al.* [2001] and Gibson *et al.* [2002]. As recommended and concluded by ACI 374.2R-13, the normal loading history has two significant parameters, which are the increment and the number of cycles at each deformation level. Priestley [1987] used an increasing loading history, and the increment is the first yield displacement with two cycles at each level. In Aboutaha *et al.* [1999] tests, the increment was particularly chosen at drift ratio of 0.5%, which was the same as Mo *et al.* [2000]. Different loading history is employed for different objectives. These incorporate near-field effects, which was rested by Orozco *et al.* [2002]. Loh *et al.* [2002] pointed out that the permanent displacement was not obvious in the pseudo-dynamic test. Kawashima *et al.* [1998], Phan *et al.* [2007], and Hoon Choi *et al.* [2010] concluded that large residual displacement on one side of the columns could be generated by the near-fault ground motions. Hoon *et al.* [2010] reported that the ductility capacity and measured plastic hinge lengths for columns under near-fault earthquakes were similar to that under far-field earthquakes. Recently, a study by Yi *et al.* [2012] found both the axial loading value and the loading path have influences on the length of the plastic hinge region along the columns. Generally, it was concluded that although a significant number of dynamic tests have been conducted on the column specimens, far fewer tests were performed to discuss the seismic behaviors of the columns under pulse-like motions.

Current seismic design criteria in provisions for RC columns which were mainly developed based on far-field ground motions. The general standard loading sequence cannot represent the influence of near-fault ground motion on the structural performance. The difference between the near-fault ground motion and far field ground motion lies in the different sequence of the peak loading arriving in the loading cycles. Based on the characteristics of the near-fault seismic displacement demand, a particular loading pattern was designed to simulate several cyclic peaks in the early stage of the loading history. The new loading sequence may result in different findings about the characteristic of stiffness degradation, energy dissipation, confined stress, etc. Three RC circular column specimens were tested under reversed cyclic loading to investigate the impact of different loading histories on seismic behavior of the columns.

2. Experimental Procedure

2.1. *Specimen Design*

Three specimens were designed in the Structural Laboratory of Hunan University. The columns had a clear height of 2400 mm with a cross section of 370 mm. The outer surface

TABLE 1 Column specimen test parameters

Specimen	Transverse Reinforcement	Longitudinal Reinforcement	Concrete strength* f_u (MPa)	Axial Compression Ratio	Axial load (kN)
L-1	Circular Hoops D = 10mm	8 × HRB400 D = 14mm	48.08	38.7%	1600
L-2	$f_y = 468$MPa	$f_y = 421$MPa	43.05	43.2%	1600
L-3	$f_u = 615$MPa	$f_u = 543$MPa	52.44	35.4%	1600

*Notes: Based on specifications in the Chinese design code of concrete structures, the axial compressive strength of the concrete cylinder is approximately 80% of the cube compressive strength, and the data were measured from cub compressive strength.
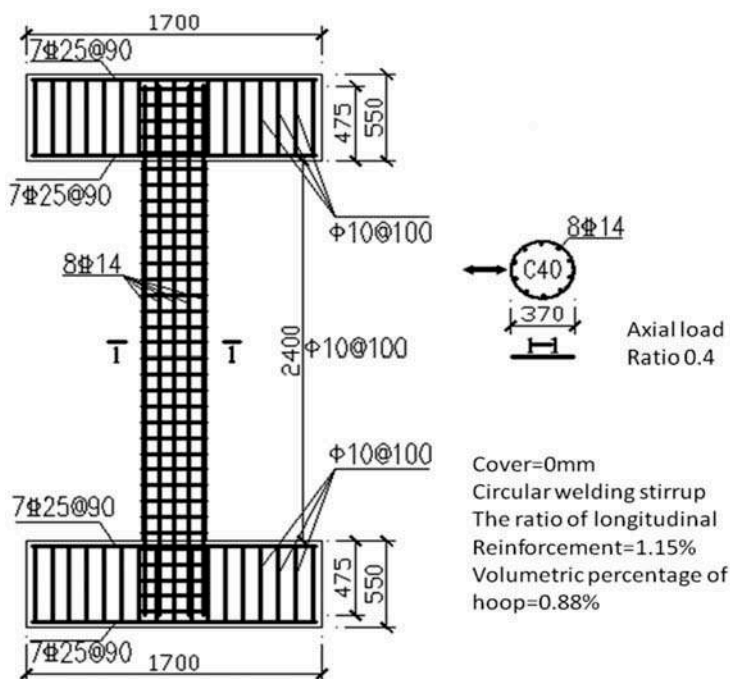
FIGURE 1 Specimen details.

of the transverse reinforcement was exposed to air. The exposure made strain gauge installation much easier and ensured the quality of installation. The details of the experimental parameters and reinforcement instrumentation were shown in Table 1 and Fig. 1. Three columns were reinforced with eight HRB400 (GB50010-2010; China Code for design of concrete structures, 2010) longitudinal reinforcing bars (diameter $\Phi = 14$ mm) with a yielding strength f_y of 421 MPa. The total longitudinal reinforcement ratios of columns were 1.15%, while the transverse reinforcement consists of HRB235 steel hoops (diameter $\Phi = 10$ mm, spacing = 100 mm, transverse reinforcement ratio is 0.9%).

2.2. Test Setup

With large-scale testing facility, the tests were conducted at the Structural Laboratory of Hunan University as shown in Figs. 2 and 3. The top and bottom stubs of the column specimen were post-tensioned to an L-shape loading arm and the reaction floor beam by eight tie-down rods, respectively. The cyclic lateral loading was applied by a German SCHENCK actuator, which was connected to the L-shape loading arm with the inflection point occurring at its mid-height. The loading actuator has a capacity of 630 kN and a stroke of 500 mm in both positive and negative directions. The unbalanced moment caused by eccentric loading of the beam itself was balanced by two US MTS vertical actuators, which have a capacity of 1000 kN and a stroke of 500 mm. Two vertical actuators applied a constant axial force 1600 kN on the loading beam and kept it parallel to the base by adjusting vertical displacements. All the servo actuators have internal LVDTs and load cells, and the hysteretic curve data were auto-recorded by data acquisition system of the MTS controller. An amendment was applied in the test, in which the lateral component of the axial load has been subtracted from the lateral load.
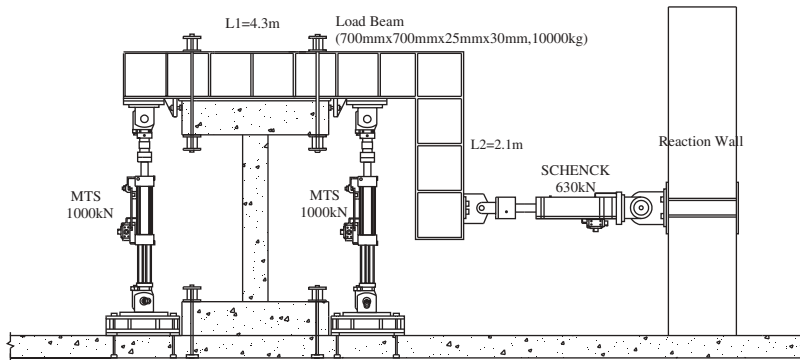

FIGURE 2 Illustration of test setup.
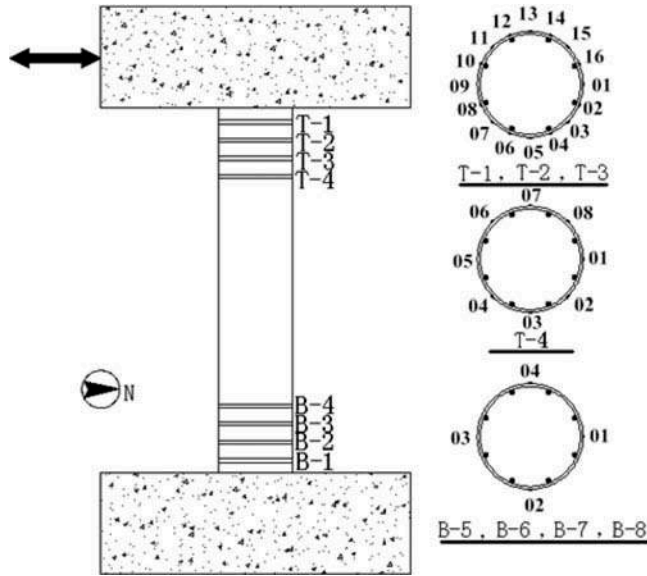

FIGURE 3 Test setup picture.

FIGURE 4 Strain gauge details.

2.3. Instrumentation

During the test, the bottom rigid stub of the specimen was mounted by the steel beams and bolts. The corresponding relative displacements between footing and floor were measured by two TML TDP-10 displacement transducers. In the potential plastic hinge region, strain gauges were installed along the circumferential direction of the hoops as shown in Fig. 4. In total 72 strain gauges were utilized to measure transverse deformation and the hoop strain. For example, T-1-9 denotes the strain gauge located at the 9th point along the first circular hoop at the top (T) end of the column.

Ten displacement transducers were mounted at the footing of the column to measure the bending deformation, shear deformation, and bonding-slip deformation. The instrumentation layout of the displacement transducers in plastic hinge region was shown in Fig. 5. Embedded bolts extended 100 mm depth into concrete core, and the displacement transducers were attached between them. Thus, the curvature and shear deformation in plastic hinge can be calculated by Eqs. (1)–(2):

$$\Phi_i = \frac{(\Delta_{Li} - \Delta_{Ri})}{L_i H_i} \tag{1}$$

$$\gamma = \frac{\sqrt{2}\Delta}{h}. \tag{2}$$

In which Φ denotes curvature; Δ_{Li} and Δ_{Ri} are measured deformation of the column by left and right displacement transducers; H_i means the distance of adjacent embedded bar at each level; L_i denotes the distance between displacement transducer center line at different level; γ is shear deformation; Δ means elongation value of inclined displacement transducer; and h means the height of shear strain measurement region.
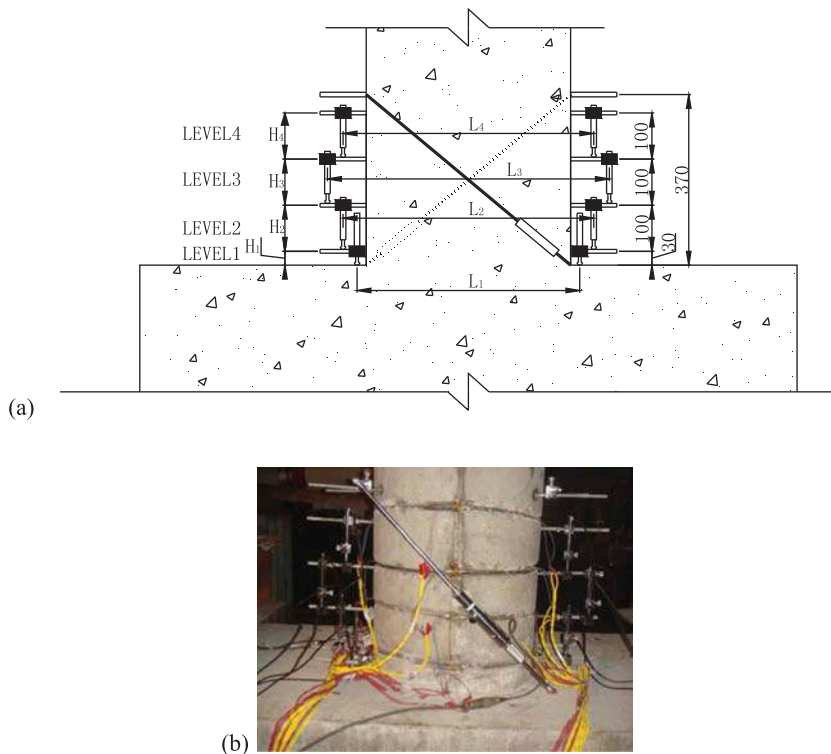
FIGURE 5 (a) Displacement transducer instrumentation layout (units: mm) and (b) instrumentation picture. (This picture only shows one inclined gauge.)

2.4. Loading Program

The specimens were tested by using displacement control. Three types of loading procedures were used for different specimen, as shown in Fig. 6. Lateral load reversals in push and pull directions were symmetric. The purpose for designing L-1 was used to estimate the drift ratio. L-1 was applied increasing cyclic lateral loading as shown in Fig. 6a, so as to measure the ductility of the column designed under current seismic code. In each drift ratio, the constant cycle repeated twice. L-2 and L-3 were subjected to opposite loadings to study the seismic performance of columns under different loading histories which were shown in Fig. 6b–c. As to L-2, the amplitude of the first 14 cycles was upgraded from 0.5% to 2% in the loading pattern by an increment of 0.25%. However, a reversed sequence was applied to L-3. Specimens subjected to subsequent cyclic lateral loading were found with an equivalent 2% drift ratio. The equal loading sequences were designed to investigate the residual seismic performance. L-2 and L-3 are to be mainly focused on the following content.

3. Experimental Observations

3.1. Specimen L-1

The yielding load of Specimen L-1 reached 171.53 kN at the drift ratio of 0.75% during the 3rd cycle. When the drift ratio firstly reached 1% (24 mm), several flexural cracks parallel to the base with maximum width of 0.13 mm were appeared at the tension side of the
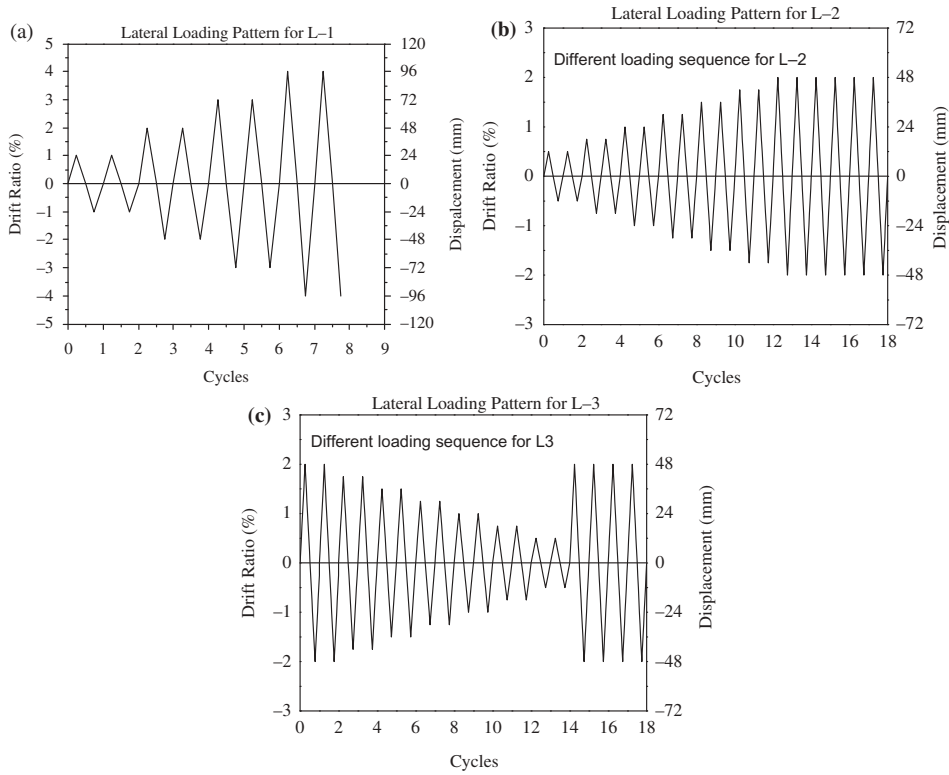
FIGURE 6 Loading programs for different specimen.
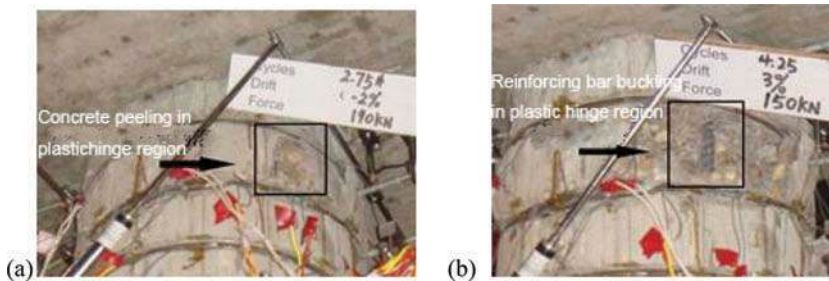
FIGURE 7 Experiment phenomenon of column L-1: (a) concrete spalling in plastic hinge region and (b) reinforcing bar buckling in plastic hinge region.

plastic hinge. Meanwhile, the concrete between adjacent hoops was spalling. Thereafter, local buckling near the footing and more spallings of the concrete were found at the drift ratio of 2% (48 mm). When the first cyclic peak value reached 3% (72 mm), the transverse strength decreased dramatically to 83% of the peak strength. A significant buckling with severe spalling of the core concrete was presented with the longitudinal reinforcement in compression region of the plastic hinge. Meanwhile, the vertical loading capacity of the specimen was lost after the buckling of the longitudinal reinforcement. Finally, the drift ratio approximately reached around 3% when the specimen reached the ultimate limit state of the capacity. Meanwhile the displacement ductility ratio reached around 4.48. The typical experiment observations of column L-1 is shown in Fig. 7.

3.2. Specimen L-2

The yielding load and yielding drift ratio of Specimen L-2 reached 160.7 kN and 0.62% (14.9 mm) at the drift ratio of 0.75%, respectively. During the 2nd cycle at the drift ratio of 2%, the lateral strength dropped down to 79% of the maximum strength in both directions of loading. The loading steadily increased with the decrement of the lateral strength. Thereafter, the transverse strength decreased to 55.8% of the peak strength after the drift ratio reached 2%. Meanwhile, the vertical capacity was lost when the longitudinal reinforcement near neutral axis was buckled. Finally, the failure pattern is almost the same as specimen L-1.
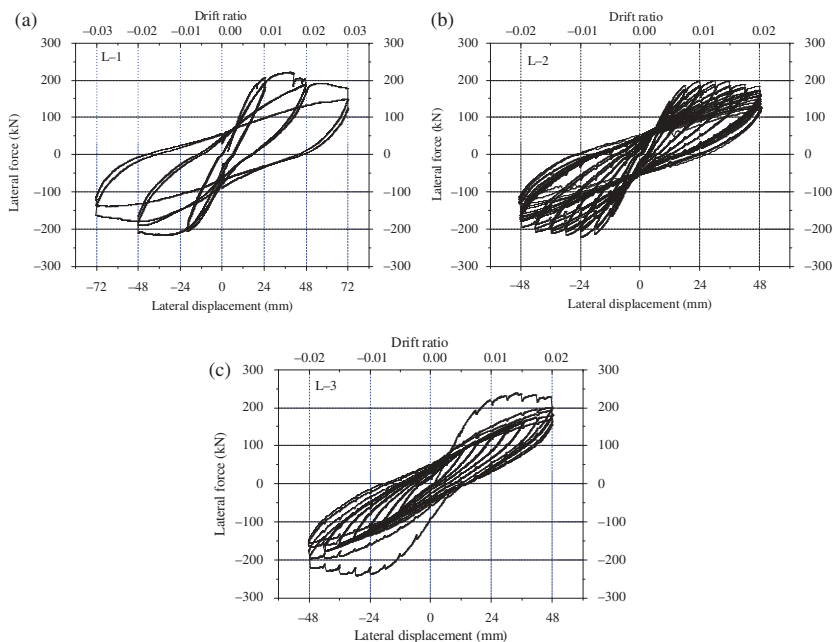
3.3. Specimen L-3

The yielding load and yielding drift ratio of Specimen L-3 were 179.7kN and 0.65% (15.7 mm) respectively. When the first cycle at the drift ratio 2% (48 mm) was reached, peeling and crushing of the core concrete occurred near the compression side in plastic hinge. After the first cycle at the drift ratio 2%, the transverse strength in both directions reduced to 75.6% of the maximum strength in two directions. The decreased loading sequence was applied to the specimen after the peak cycle appeared, specimen performed well without any new cracks or spallings occurred in this loading sequence. During the 2nd constant cycle of 2%, the lateral capacity of the maximum strength was dropped down to 67.8%. Then the vertical capacity of the specimen was lost at the same time. There was no significant difference between L-1 and L-2 when failure occurred following the buckling of the longitudinal reinforcement.

## 4. Analysis of Deformation and Energy

4.1. Hysteretic Curves and Envelope Curves

The lateral force-displacement hysteretic responses and the corresponding envelopes of different specimens are shown in Figs. 8–9. As shown in Fig. 8, all the specimens were stably exhibited with hysteretic characteristics. Shapes of the hysteretic loops were full without obvious appearance of shear cracks before the buckling of the longitudinal reinforcement. The dispassion of the energy was mainly caused by the tension and compression the material. This indicated reasonably satisfactory energy absorption properties. Linear response was showed with L-1 and L-2 at the initial loading stage, and the yield point reached at the drift ratio of 0.01 (total displacement equals 24 mm). A slightly increase in the load carrying capacity was evident because of strain hardening, and the maximum applied horizontal force was reached, thereafter, the load dropped fast following the buckling of the longitudinal bar and the crushing of the concrete. L-1 lost its capacity at the drift ratio of 0.03 with less hysteretic loops, while L-2 presented much more loops which demonstrated good ductility under the corresponding loading sequence. L-3 was subjected to the decreasing displacement loading sequence, and the yield point and strain hardening stage appeared when the first cyclic load was reached.

The envelope curves of three specimens were demonstrated in Fig. 9. In the figure it can be found that the force increased linearly with the drift ratio at the beginning stage, and the increasing indicated that each specimen behaved in its elastic stage. With the increasing of the drift ratio, the lateral force decreased with the increment of the displacement. The shapes of three envelope curves matched well in the elastic stage, however, L-3 reached a

FIGURE 8 Hysteretic curves of three specimens: (a) Specimen L-1, (b) Specimen L-2, and (c) Specimen L-3.
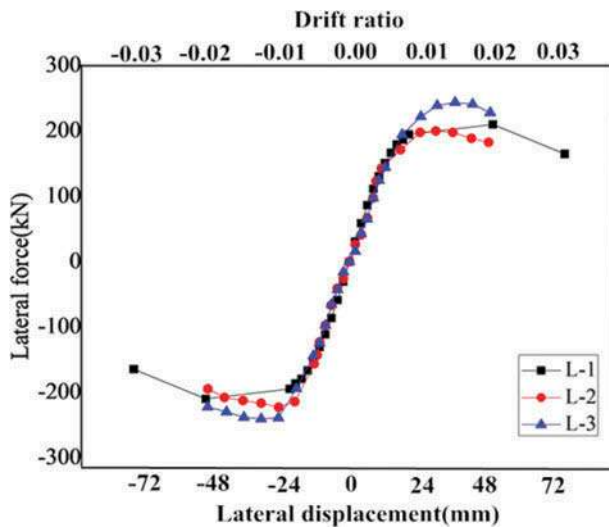
FIGURE 9 Envelope curves of three specimens.

slightly larger lateral force which may be resulted from the largest concrete strength existed in the specimen. Additionally, a relatively larger drift ratio was presented with L-1 which is due to the specific loading sequence.

4.2. Stiffness Degradation

The research on the degradation of stiffness is important to the seismic performance of the column under reversed cyclic loading. To investigate the degradation of column's stiffness, average secant stiffness is defined as Eq. (3):

$$K_{ji} = \sum_{i=1}^{n} V_{ji} / \sum_{i=1}^{n} \Delta_{ji},$$ (3)

in which K_{ji} means the average secant stiffness at the jth amplitude in loading history; V_{ji} denotes the force recorded in ith cycles at jth amplitude; and Δ_{ji} is the displacement in ith cycles at jth amplitude. Average secant stiffness of L-2 and L-3 are compared in Fig. 10, in which the positive and negative value denoted the average secant stiffness of the first few cycles in the loading history. The initial values are different in the positive and negative directions, which caused the loading sequence as well as the eccentric loading axial force. At the beginning stage before the drift ratio at 1%, there was a large difference between the average secant stiffness of L-2 and L-3. The difference may result from the different confining stress of the two specimens. In the constant loading procedure, the average secant stiffness remained almost the same. Although L-2 and L-3 were subjected to different loading sequences, the average secant stiffness was gradually approaching after the 15th cycle. From this figure it was demonstrated that the sequence appears of the displacement peak value was showed no obvious influence on the secant stiffness.

4.3. Lateral C

The failure pattern of the specimens was dominated by the buckling of longitudinal bars and the crushing of the compression concrete dominated the failure pattern of the specimens. The lateral load capacity of L-1, L-2 and L-3 were 220kN, 200kN and 230kN respectively. A comparison was made between L-2 and L-3. Both specimens achieved their lateral load capacity at the same drift ratio (1.5%) within different cycle sequences. The residual
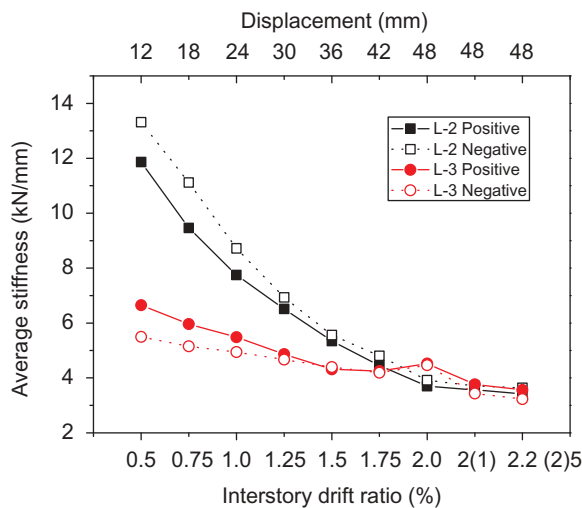

FIGURE 10 Decrement of average secant stiffness with drift ratio.

stiffness of the column remained almost the same at the end of the reversed sequence load-ing. When the constant amplitude cycles the stiffness of L-3 quickly decreased, the failure occurred after the 2nd constant cycle at the drift ratio of 2%, however, the failure occurred after 5 constant cycles at the same loading level for L-2. The difference demonstrates that the sequence in loading history has an important influence on the lateral capacity of the columns. It can be inferred that the peak loading appears in the early stage of the loading history would lead to an earlier buckling of the longitudinal bars.

4.4. Energy Dissipation Analysis

Energy was continually dissipated in the reversed cyclic loading procedure. The enveloped area between the loading curve and the displacement axis denotes the amount of absorbed energy, while the amount of dissipated energy in the specimen was indicated by the enveloped area between the unloaded curve and displacement axis. In the enveloped area of A-B-C-D-E in Fig. 11, one hysteretic loop denotes the amount of dissipated energy of the specimen in one reserved cyclic loading procedure. The cumulative energy dissipation curves of L-2 and L-3 were shown in Fig. 12. It can be found that the paths of the curves were different due to the first 14 cycles were different. At the 16th cycle, the cumulative
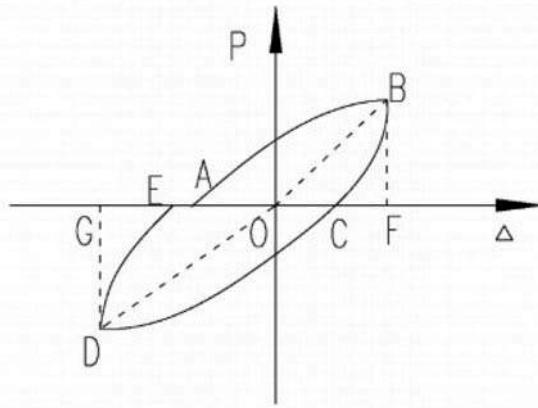

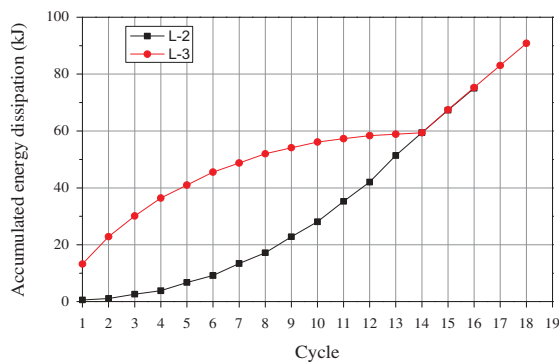**FIGURE 11** Demonstration of hysteretic loop.

FIGURE 12 Cumulative energy dissipation curves for L-2 and L-3.

energy dissipation curves almost coincided; however, the energy dissipation ability for L-2 was much better than L-3. It was found that L-3 lost its capacity at the 16th cycle, while L-2 still maintained its lateral capacity until the 19th cycle. It was clearly showed that the sequence of the loading history is critical to the energy dissipation capacity.

5. Stress and Strain Analysis

5.1. Distribution of Hoop Strain

The hoop strain along the height of the column is illustrated in Fig. 13, in which the strains nearby the bottom and the top end of the specimens are plotted, respectively. The y-coordinate means the strain gauge number and the distance from the position of the measurement point to the end of the column. X-coordinate means the magnitude of strain in the hoops. It was clearly showed that in the figure the maximum hoop strain located at 180 mm away from the bottom end of the column, and the finding was almost identical with the test observations of Xiao *et al.* [1998]. The strain along L-2 is increased with the increment of loading drift ratio. When the loading drift ratio was less than 1.5% in Fig. 13a, the maximum hoop strain appeared at T-1 and B-1 around the end of the specimen began to reach yield strain ($2300\mu\varepsilon$). When the drift ratio reached 1.75%, the strain along T-2 and B-2 will dramatically increase beyond the strain along T-1 and B-1. The fact demonstrated the buckling of the longitudinal bar occurred at the corresponding location. When the drift ratio reached 2%, T-2 hoop strain increased with the increment of the cycles, which is caused by the deformation of the concrete as well as the yielding of the longitudinal bar. As to L-3, the hoop strain decreased with the decrement of the drift ratio after the peak drift
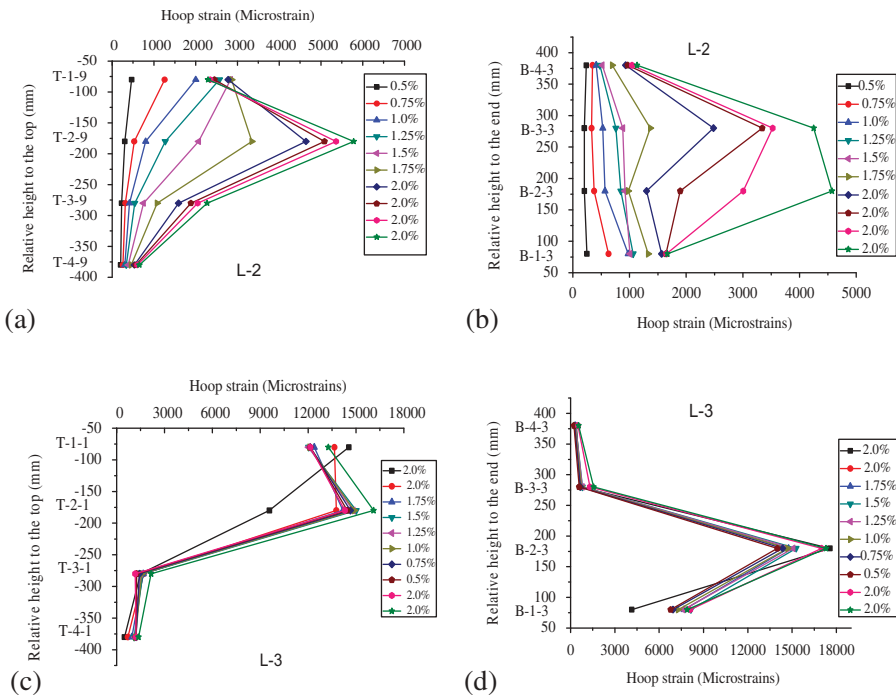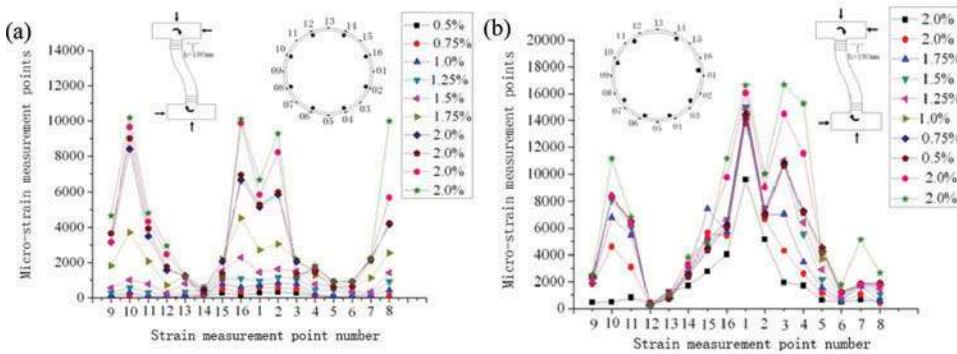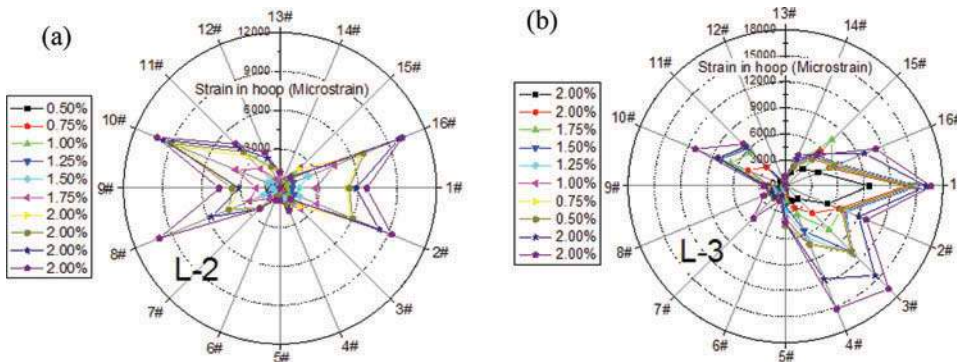

FIGURE 13 Distribution of hoop strains along the height of columns.

FIGURE 14 (a) Circumferential strain of Column L-2 in location T-2 and (b) circumferential strain of Column L-3 in location T-2.

FIGURE 15 Circumferential distribution of T-2 hoop strain (a) L-2 and (b) L-3.

ratio was exceeded, however the rate of descent is in a small extent. When loaded into the constant loading sequence, the hoop strain increased once again.

T-2 strain distributions measured from the circumferentially arranged strain gauges along the hoop L-2 in each displacement increment of specimens are plotted in Fig. 14a–b. It can be seen that at the beginning, the strain distribution remained constant before the drift ratio was less than 1.25%, which means the hoops were in elastic stage. However, the hoop strain at Location 16# exceeded 2000 $\mu\varepsilon$ when the drift ratio reached 1.5%. Thereafter, the drift angle exceeded 1.75%, and the hoop strains at Locations 1#, 2#, 8#, 10#, and 16# increased quickly. It indicated the progress of cracks in core concrete as well as the buckling of the longitudinal bar, which demonstrated the increasing of confinement action of the hoop. The hoop strains at Locations 10#, 1#, 3#, and 4# still increased with the decrement of the loading amplitude when the peak loading sequence was exceeded. Finally, in the subsequent uniform loading sequence stage, the hoop strain increased once again until the experiment was ended.

The circumferential distribution of hoop stress was evaluated by measuring the stress-strain relationship in the material test. A numerical model proposed by Menegotto and Pinto [1973] was used due to the lack of cyclic test data. By substituting the measured strain data obtained from monotonic loading test into the numerical model, the circumferential distribution of confining stress was calculated and plotted in Fig. 15. The maximum confining stress was about 2 MPa, and average value of the whole section was around 1.5 MPa. Under this confining stress level, the compressive strength of concrete was estimated to increase

by 15–20%. The ductility of specimen was significantly improved by the lateral confining stress although the increment of the concrete strength had less influence on the loading capacity of column.

5.2. Confining Stress Analysis of Section

Based on Mander's confinement model, a certain relationship was found between the ultimate limit strength and the confining stress of the section. The confining stress in the core concrete can be solved if the tension force of the hoops are available based on the force equilibrium condition. The average confining stress proposed by Mander *et al.* [1988] was shown as Eq. (4) in Fig. 16:

$$f_l = \frac{(f_{s1} + f_{s2})A_s}{Sd_s}. \tag{4}$$

In which f_l means the average confining stress in the section; f_{s1} and f_{s2} are hoop stress; A_s denotes the area of hoop strain; S is the distance of hoops; and d_s is the diameter of the section centerline. The hoop stress was deduced from the measured hoop strain based on "Steel02" stress-strain model, which was proposed in Opensees [Open System for Earthquake Engineering Simulation, 2008], as shown in Fig. 17.
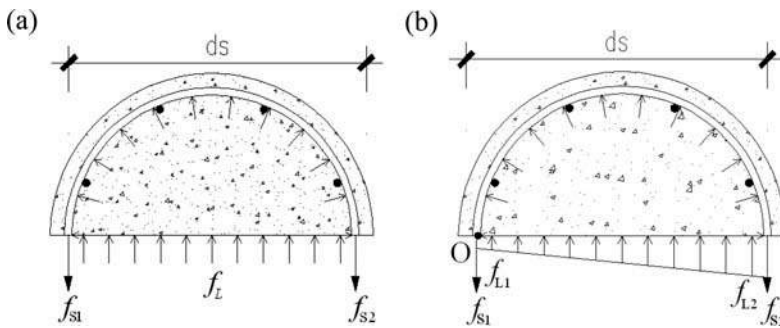
FIGURE 16 (a) Mander's average stress model and (b) confining stress based on equilibrium condition.
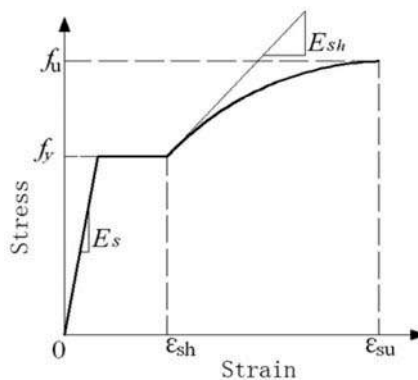
FIGURE 17 Stress-strain constitutive model of steel.

The tension force is non-uniformly distributed along the hoop. As to simplification, the confining stress is assumed to be linearly distributed in this article. Based on the force and moment equilibrium conditions, two equations can be deduced as Eqs. (5) and (6):

$$\frac{1}{2}(f_{L1} + f_{L2})Sd_s = (f_{s1} + f_{s2})A_s \tag{5}$$

$$\frac{1}{2}f_{L1}Sd_sd_s + \frac{1}{3}(f_{L2} - f_{L1})Sd_sd_s = f_{s2}A_sd_s. \tag{6}$$

The confining stress distributions were demonstrated in Figs. 18–19 when the drift ratio equals +1% and ultimate state separately. In these figures, the encoding No. N# is the same as the number shown in Fig. 4. The value after the encoding No. N# shows the hoop stress. Based on the results above, it can be concluded that the hoop stress is non-uniformly distributed across the whole section. The hoop stress value is larger in compression section especially nearby the longitudinal bars, while around neutral axis it is pretty small. The calculated confining stress is 2.04 MPa after the measured yielding strain of the hoop was substituted into Mander's equation. In these figures, it was found the average confining
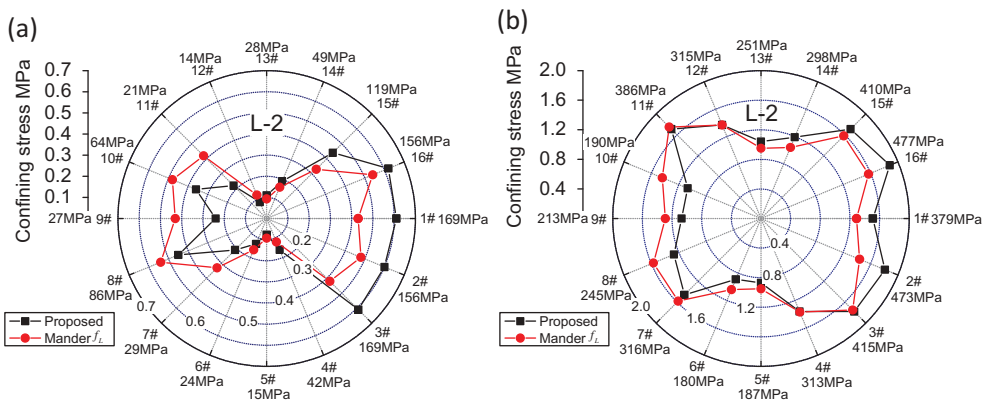
FIGURE 18 The circumferential stress distribution of T-2 in L-2 specimen (a) drift ratio equals +1% and (b) drift ratio equals +2%.
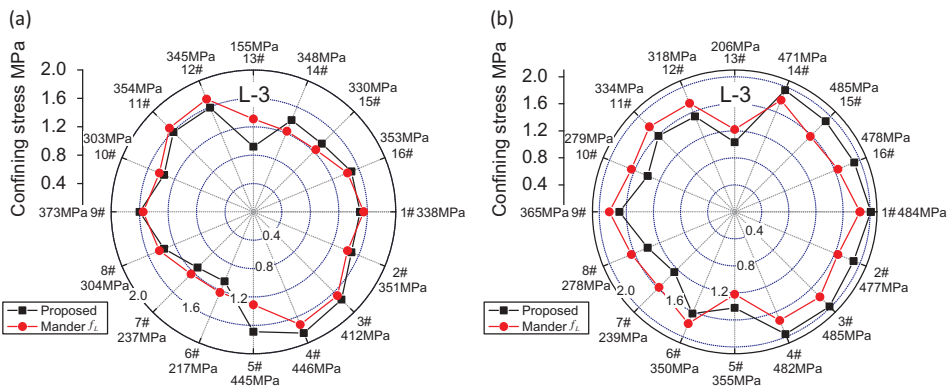
FIGURE 19 The circumferential stress distribution of T-2 in L-3 specimen: (a) drift ratio equals +1% and (b) drift ratio equals +2%.

stress is less than analytical confined stress (2.04 MPa) calculated by Mander's equation, which may result from the hoop stress is non-uniformly distributed due to eccentric compression on the section, both sides of which can hardly reach the yielding strength.

6. Plastic Hinge Analysis
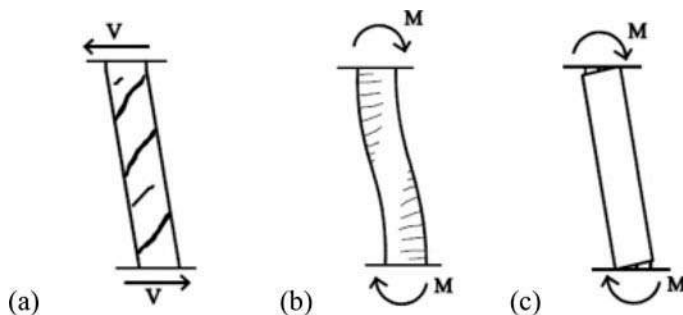
6.1. Length of the Plastic Hinge

Generally, there are two methods for measuring the length of plastic hinge. The first one is to directly measure the length of the spalling concrete at top and bottom end of the column, and the second one is to utilize inverse analysis to estimate the length of the plastic hinge at either the yielding point or the ultimate point in terms of the force-displacement envelope curve [Pam, 2009; Paulay, 1992]. In Fig. 20, it can be found that the height of spalling concrete in plastic hinge region of L-2 and L-3 are almost identical. At the end of loading experiment for L-2, quite a few small cracks were found within 100 mm length outside the plastic hinge L-3 remained intact without any cracks at the same region. In Table 2, the average calculating plastic hinge length for L-2 was 108.3 mm while L-3 was only 100.8 mm, which showed the flexure failure dominated the failure of RC column. At the same time the appearance of the largest displacement in the loading procedure showed less influence on the length of the plastic hinge. The calculated length of the plastic hinge was only about half of which estimated by different scholars since the length of the plastic hinge related to ultimate displacement. The proposed analytical formula was derived for length of plastic hinge calculation based on a gradual increasing loading procedure until the failure occurred, while the loading patterns used in this article were different, so it resulted in

(a) Upper end of column L-2   (b) Bottom end of column L-2

(c)Upper end of column L-3   (d) Bottom end of column L-3

FIGURE 20 Demonstration of the length of plastic hinge.

TABLE 2 Length of plastic hinge (mm)

| Specimen | Upper end | | Lower end | | Average | | | |
	Observed value	Inversed analysis value	Observed value	Inversed analysis value	Inversed analysis value	Inversed analysis value	Park (1994)	Priestley (1992)
L-2	180	114.5	200	102	190	108.2	180	226
L-3	180	94.3	200	107.2	190	100.7		

FIGURE 21 Demonstration of deformation component: (a) shear deformation, (b) bending deformation, and (c) bonding-slip deformation.

underestimating the ultimate drift ratio. The calculated length of the plastic hinge was less than which calculated by the empirical formula, and it was also verified by El-Bahy and Kunnath [1999]. The measured lengths for L-2 and L-3 were pretty close, indicating the sequence appearance of the maximum loading cycle has no obvious relationship with the length of plastic hinge.

7. Deformation Analysis

The measured deformation of the specimen is composed of such three deformation components as shear deformation (Fig. 21a), bending deformation (Fig. 21b) and bonding slip deformation of the longitudinal bar (Fig. 21c) due to the rotation of the bottom column. The total deformation of the RC columns was dominated by three kinds of deformations under the cyclic loading.

7.1. Shear Deformation Component

The displacement transducers were instrumented in plastic hinge region to measure shear deformation. The equation for calculating diagonal cracking load of RC column was shown in Eqs. (7)–(9) [Halil Sezen, 2006]. The cracking load of diagonal crack for L series column will reach 326.1 kN, which is far beyond the peak loading of the specimen. In the experiment there were no more diagonal cracks appeared, and the specimen presented classic bending failure mode. In this article, the shear deformation just occupied a small part of the total deformation, which can be considered together with bending deformation:

$$V_{cr} = \left(\frac{P}{50000} + 0.0062 \right) \frac{GA}{L} \tag{7}$$

$$G = 0.4E_c \tag{8}$$

$$E_c = 4730\sqrt{f_c'}. \tag{9}$$

In which, V_{cr}, P, G, L, A, E_c, f_c', respectively, denote the cracking load of the diagonal cracks, axial force, shear stiffness, height of the column, cross-section area, elastic modulus of concrete, and cylinder compression strength. Here, the cylinder compression strength was chosen as 0.8 times of cubic compression strength.

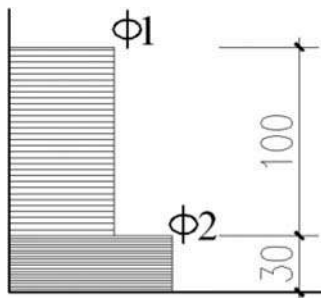### 7.2. Bonding-Slip Deformation Component

Bonding-slip deformation is caused by the slip of the longitudinal bar from the footing. The deformation would result in the rotation of the column as a rigid body. The instrumentation for displacement transducer was shown in Figs. 5 and 22. LVDTs were utilized to measure the deformation on both sides of the section, and the average curvature of the section, which is considered to be uniformly distributed along the measurement height. The curvatures were calculated by Eqs. (10)–(11):

$$Level\,1\ \ \Phi_1 = \frac{(\Delta_{L1} - \Delta_{R1})}{L_1 H_1} \tag{10}$$

$$Level\,2\ \ \Phi_2 = \frac{(\Delta_{L2} - \Delta_{R2})}{L_2 H_2}. \tag{11}$$

In which, Δ_{L1}, Δ_{L2}, Δ_{R1}, and Δ_{R2} mean the corresponding deformation measured by LVDTs on right or left at first level and the second level to the footing; Φ_1 and Φ_2 are corresponding curvatures at first level and the second level; H_1 and H_2 means the distance of adjacent embedded bar at 1st and 2nd level; and L_1 and L_2 denotes the distance between LVDT center line at first and second level the center horizontal distances of LVDTs on both sides. Curvature measured at level 1 contains both the flexural curvature and the bonding-slip induced curvature. Considering the relative small length of level 1, the flexural curvature can be separated by subtracting the measured curvature at level 2. The bonding-slip rotation can then be estimated by Eq. (12):

$$\theta = H_1\left(\Phi_2 - \Phi_1\right), \tag{12}$$

FIGURE 22 Bonding-slip measurement: (a) instrumentation of the displacement transducer and (b) curvature distribution.
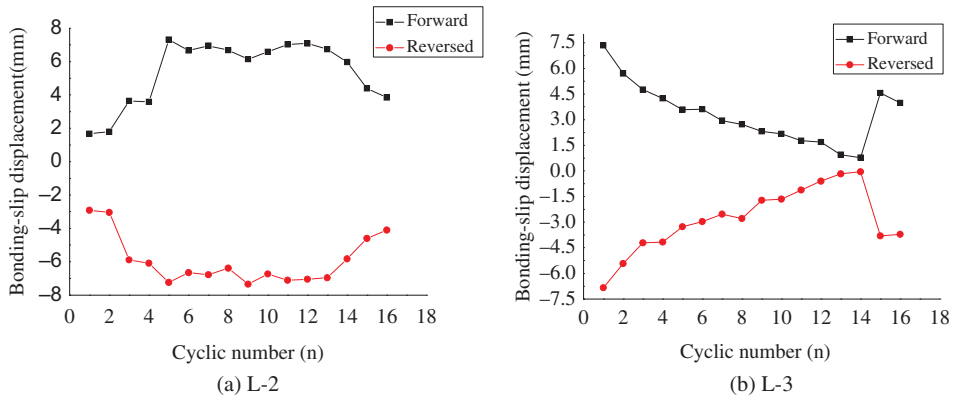
FIGURE 23 Bonding-slip deformation envelope curve (a) L-2 and (b) L-3.

in which θ means the rotation at the end of the column. After the rotation of both ends of column has been calculated, the bonding-slip displacement component can be expressed as Eq. (13):

$$\Delta_{slip} = \frac{(\theta_{slip,top} + \theta_{slip,bottom})L}{2}.$$
(13)

In the equation, Δ_{slip} means bonding-slip displacement, $\theta_{slip,top}$ and $\theta_{slip,bottom}$ are rotation angles at both ends of the column, and L means the height of the column.

In Fig. 23 it can be found that the measured bonding-slip displacement has similar trend with the lateral loading. The similarity lies in the bonding effect of the longitudinal bar generated by the cyclic reversed loading. In other words, the stress of the longitudinal bar has linear relationship with the amount of unplug effect of the rebar.

7.3. Bending Deformation Component

In this article, the bending deformation component is obtained by subtracting the bonding-slip deformation from the total deformation as shown in Eq. (14):

$$\Delta_f = \Delta_{total} - \Delta_{slip}.$$
(14)

The bending deformation for L-2 and L-3 are shown in Fig. 24. Although the total deformation is constant in uniform loading sequence, the bonding-slip deformation decreased with the decrement of bonding-slip deformation. The difference indicated that the bending deformation actually increased with the increment of the curvature in plastic hinge. The increment of the curvature will result in the increment of concrete and steel strain. Thus, the member failed via the accumulated damage in the member.

8. CONCLUSIONS

Three RC circular column specimens without an effective concrete cover were tested under constant axial compressive and cyclic lateral loading. The seismic behavior of the specimens under different loading paths is examined to study the influence of displacement
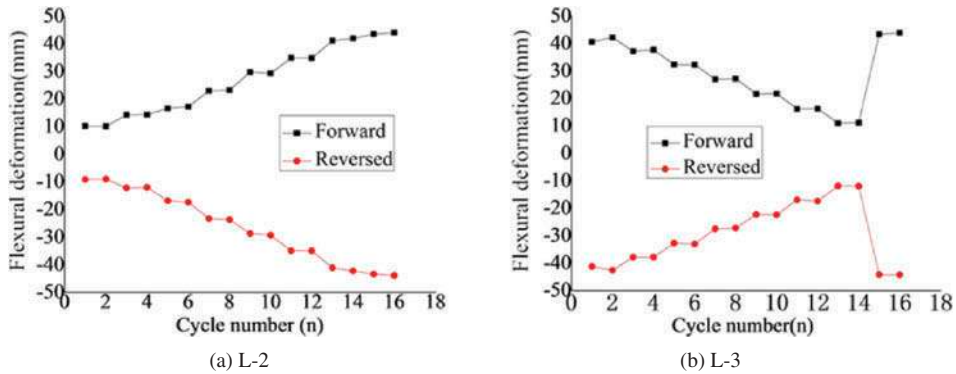
FIGURE 24 Flexural deformation envelope curve (a) L-2 and (b) L-3.

history sequence on the seismic behavior of the columns. Based on the analysis results and comparisons with theoretical predictions, the following conclusions were reached.

1. The limit drift angle of L-1 is 3% and the displacement ductility factor is 4.47. The fact demonstrated that a lack of ductility reserve would be led by the RC frame columns designed based on current Chinese seismic code will lead to a lack of ductility reserve. As for L-3, the average secant stiffness under the gradually decreased loading sequence after the peak loading is close to the average secant stiffness at the peak loading. Compared with the average secant stiffness of L-2, the secant stiffness of L-3 corresponding to the non-peak loading is obviously less than which of L-2. However, the secant stiffness of L-2 and L-3 at the peak loading is almost the same, which shows the secant stiffness at the peak loading has no obvious relationship with the sequence of appearance of the peak loading. In addition, the cumulative energy dissipation ability was independent to the sequence of appearance of the peak loading.

2. From the top and bottom end of the column, the maximum strain in plastic hinge region generally appears at the height of the half column diameter. The length of plastic hinge relies on the limit displacement, so the length of the plastic hinge for L-2 and L-3 are obviously less than the calculation value by empirical equations. However, the calculated length of the plastic hinge of these two specimens is almost identical. The sequence of appearance of peak loading is independent to the length of plastic hinge.

3. Due to the eccentric compression of the section, both sides of the hoop stress can hardly reach yielding stress. The actual confinement stress of the specimen was overestimated by the calculated confinement stress based on Mander's equation.

4. Three kinds of deformations were separated from the total deformations of the RC columns under the cyclic loading. One similar trend was found between the measured bonding-slip displacement and the lateral loading. The similarity lies in the bonding effect of the longitudinal bar generated by the cyclic reversed loading. The bending deformation actually increased with the increment of the curvature in plastic hinge.

Funding

References

Aboutaha, R. and Machado, R. [1999] "Seismic resistance of steel-tubed high-strength reinforced-concrete columns," *Journal of Structural Engineering* **125**(5), 485–494.

ACI-Committe-374 [2013] *Guide for Testing Reinforced Concrete Structural Elements under Slowly Applied Simulated Seismic Loads* (ACI 374.2R-13), American Concrete Institute, Farmington Hills, Michigan.

Austin, B. [2009] "Investigation of near-fault ground motion effects on substandard bridge columns and bents," Ph.D. thesis, University of Nevada, Reno, Nevada.

Bahy, A. E. and Kunnath, S. K. [1999] "Cumulative seismic damage of circular bridge columns: benchmark and low-cycle fatigue tests," *ACI Structural Journal* 96(5), 633–641.

Bahy, A. E. and Kunnath, S. K. [1999] "Seismic energy based fatigue damage analysis of bridge columns: variable amplitude tests," *ACI Structural Journal* **96**(5), 711–719.

Chopra, A. K. and Chintanapakdee, C. [2001] "Comparing response of SDOF systems to near-fault and rar-fault earthquake motions in the context of spectral regions," *Earthquake Engineering and Structural Dynamics* **30**, 1769–1789.

Erol, K. and Sashi, K. K. [2006] "Effects of fling step and forward directivity on seismic response of buildings, *Earthquake Spectra* **22**(2), 367–390.

Gibson, N., Filiatrault, A., and Ashford, S. [2002] "Impulsive seismic response of bridge column-cap beam joints," *ACI Structural Journal* **99**(4), 470–479.

Hwang, T. H. [1984] "R/C Member cyclic response during various loadings," *Journal of Structure Engineering* **110**(3), 477–489.

Hamilton, C. H., Pardoen, G. C., Kazanjy, R. P., and Hose, Y. D. [2001] "Experimental and analytical assessment of simple bridge structures subjected to near-fault ground motions," *The International Conference of Engineering Mechanics and Computation*, Cape Town, South Africa, pp. 993–1000.

Hoon, C., Saiidi, M. S., Paul, S., and Saad, E. A. [2010] "Experimental study of reinforced concrete bridge columns subjected to near-fault ground motions," *ACI Structural Journal* **107**(1), 209–213.

Hall, J. F., Heaton, T. H., Halling, M. W., and Wald, D. J. [1995] "Near-source ground motion and its effects on flexible buildings," *Earthquake Spectra* **11**(4), 569–605.

Kawashima, K., MacRae, G. A., Hoshikuma, J., and Nagaya, K. [1998] "Residual displacement response spectrum," *Journal of Structural Engineering* **124**(5), 523–530.

Liu, Y. [2010] "Seismic performance of reinforced concrete columns under near-field earthquake," Master degree thesis, Hunan University, Changsha, China.

Loh, C. H., Wan, S., and Liao, W. I. [2002] "Effects of hysteretic model on seismic demands: consideration of near-fault ground motions," *Journal of the Structural Design of Tall Buildings* **11**, 155–169.

Mander, J. B., Nigel Prisetley, M. H., and Park, R. [1988] "Theoretical stess-strain model for confined concrete," *Journal of Structural Engineering*, **114**(8), 1804–1826

Menegotto, M., and Pinto, P. E. [1973] "Method of analysis for cyclically loaded reinforced concrete plane frame including changes in geometry and nonelastic behavior of elements under combined normal force and bending," *Proc. of IABSE Symposium on Resistance and Ultimate Deformability of Structures Acted on by Well Defined Repeated Loads*, Final Report, Lisbon, pp. 541–553.

Mo, Y.-L. and Wang, S. [2000] "Seismic behavior of RC columns with various tie configurations," *Journal of Structural Engineering* **126**(10), 1122–1130.

Orozco, G. L. and Ashford, S. A. [2002] "Effects of large velocity pulses on reinforced concrete bridge columns," Pacific Earthquake Engineering Research Center Report, University of California at Berkeley. (Available at http://peer.berkeley.edu/publications/peer_reports/reports_2002/0223.pdf)

Opensees [2008] "Open system for earthquake engineering simulation," Open source software (Available at http://opensees.berkeley.edu).

Pam, H. J. and Ho, J. C. M. [2009] "Length of critical region for confinement steel in limited ductility high-strength reinforced concrete columns," *Engineering Structures* **31**(12), 2896–2908

Paulay, T. and Priestley, M. J. N. [1992] *Seismic Design of Reinforced Concrete Masonry Building*, John Wiley& Sons, Inc., New York.

Pujol, A. S., Sozen, M. A., and Ramirez, J. A. [2006] "Displacement history effects on drift capacity of reinforced concrete columns," *ACI Structural Journal* **103**(2), 253–262.

Phan, V. and Saiidi, M. S. [2007] "Near-fault ground motion effects on reinforced concrete bridge columns," *Journal of Structure Engineering* **133**(7), 982–989.

Priestley, M. and Park, R. [1987] "Strength and ductility of concrete bridge columns under seismic loading," *ACI Structural Journal* **84**(1), 61–76,

Somerville, P. G. [2002] "Characterizing near fault ground motion for the design and evaluation of bridges," Third National Conference and Workshop on Bridges and Highways, Portland, Oregon, April 29–May 1.

Somerville, P. G., Smith, N. F., Graves, R. W., and Abrahamson, N. A. [1997] "Modification of empirical strong ground motion attenuation relations to include the amplitude and duration effects of rupture directivity," *Seismology Research Letters* **68**, 199–222.

Santiago, P., Mete, A. S., and Julio, A. R. [2006] "Displacement history effects on drift capacity of reinforced concrete columns," *ACI Structural Journal* **103**(2), 253–262.

Watson, S., Zahn, F. A., and Park, R. [1994] "Confining reinforcement for concrete columns," *Journal of Structure Engineering* **120**(6), 1798–1824.

Xiao, Y. and Martirossyan, A. [1998] "Seismic performance of high-strength concrete columns," *Journal of Structure Engineering* **124**(3), 241–251.

Yi, W. J., Li, P., and Sashi, K. K. [2012] "Experimental studies on confinement effect of steel hoops in concrete columns," *ACI Structural Journal* **109**(1), 3–10.